Stress fiber strain recognition by the LIM protein testin is cryptic and mediated by RhoA

Stefano Sala and Patrick W. Oakes*

Department of Cell and Molecular Physiology, Loyola University Chicago, Stritch School of Medicine, Maywood, IL 60153

ABSTRACT The actin cytoskeleton is a key regulator of mechanical processes in cells. The family of LIM domain proteins have recently emerged as important mechanoresponsive cytoskeletal elements capable of sensing strain in the actin cytoskeleton. The mechanisms regulating this mechanosensitive behavior, however, remain poorly understood. Here we show that the LIM domain protein testin is peculiar in that despite the full-length protein primarily appearing diffuse in the cytoplasm, the C-terminal LIM domains alone recognize focal adhesions and strained actin, while the N-terminal domains alone recognize stress fibers. Phosphorylation mutations in the dimerization regions of testin, however, reveal its mechanosensitivity and cause it to relocate to focal adhesions and sites of strain in the actin cytoskeleton. Finally, we demonstrate that activated RhoA causes testin to adorn stress fibers and become mechanosensitive. Together, our data show that testin's mechanoresponse is regulated in cells and provide new insights into LIM domain protein recognition of the actin cytoskeleton's mechanical state.

Monitoring Editor Alex Dunn Stanford University

Received: Mar 31, 2021 Revised: May 13, 2021 Accepted: May 21, 2021

INTRODUCTION

Cells depend on complex networks of both biochemical and mechanical signals, which contribute to normal cellular physiology, tissue development, and homeostasis (Lecuit et al., 2011; Iskratsch et al., 2014). While the general mechanisms of biochemical signaling are well defined, the mechanisms of mechanical signaling are less clear. Cells must recognize a variety of mechanical cues (e.g., tension, shape changes, pressure, and stiffness), behavior often referred to as mechanosensing, and convert those mechanical signals into biochemical signals, a process collectively called mechano-

transduction (Paluch et al., 2015). These processes can influence a diverse array of critical functions including cell spreading (Oakes et al., 2018), force generation (Prager-Khoutorsky et al., 2011), proliferation (Rauskolb et al., 2014), migration (Das et al., 2015) and differentiation (Engler et al., 2006). Correspondingly, defects in mechanical signaling are associated with various diseases including muscular dystrophies and cardiomyopathies (Heydemann and McNally, 2007), osteoporosis (Hemmatian et al., 2017), asthma (Fabry and Fredberg, 2007), and cancer progression and metastasis (Paszek et al., 2005).

The actin cytoskeleton and its associated binding proteins are key regulators of mechanical processes within and between cells (Ohashi et al., 2017; Blanchoin et al., 2014). Of the many diverse and dynamic architectures these proteins can form, two in particular play centralized roles in force transmission and mechanotransduction: focal adhesions (FA) and stress fibers (SF). FAs are complexes of ~150 proteins that couple the actin cytoskeleton to the extracellular environment, transmitting forces between the cell and the extracellular matrix (Kanchanawong et al., 2010; Zaidel-Bar et al., 2007). Those forces are generated primarily by nonmuscle myosin II motors that pull on the actin filaments in SFs, propagating the force to the FAs, where they terminate (Schwarz and Gardel, 2012; Oakes and Gardel, 2014). SFs themselves are composed of ~10–30 cross-linked actin filaments and can span tens of micrometers across the entire cell, providing overall mechanical coherence to the cell (Tojkander et al., 2012; Cai and Sheetz, 2009; Svitkina, 2018).

This article was published online ahead of print in MBoC in Press (http://www.molbiolcell.org/cgi/doi/10.1091/mbc.E21-03-0156) on May 26, 2021.

Competing financial interests: The authors declare no competing financial interests. ORCID: 0000-0001-9951-1318.

Author Contributions: S.S. and P.W.O. conceived the study, performed and analyzed all experiments, and wrote the manuscript.

 ${\tt *Address\ correspondence\ to:\ Patrick\ W.\ Oakes\ (poakes@luc.edu)}.$

Abbreviations used: CA, constitutively active; CR, cysteine-rich; DN, dominant-negative; FA, focal adhesion; FHL, four-and-a-half LIM; FL, full-length; HFF, human foreskin fibroblast; LDP, LIM domain protein; LIM, Lin-11, Isl-1, Mec-3; MEF, mouse embryonic fibroblast; PET, Prickle, Espinas, Testin; SF, stress fiber; SFSS, stress fiber strain site.

© 2021 Sala and Oakes. This article is distributed by The American Society for Cell Biology under license from the author(s). Two months after publication it is available to the public under an Attribution–Noncommercial–Share Alike 3.0 Unported Creative Commons License (http://creativecommons.org/licenses/by-nc-sa/3.0).

"ASCB®," "The American Society for Cell Biology®," and "Molecular Biology of the Cell®" are registered trademarks of The American Society for Cell Biology.

1758 | S. Sala and P. W. Oakes

As the combination of SFs and FAs serves as the primary conduit for force transmission in adherent cells, it is unsurprising that many proteins previously identified as mechanosensitive, such as alphaactinin (Le et al., 2017), talin (Haining et al., 2016), vinculin (Goldmann, 2016), and integrins (Sun et al., 2016), are found in these structures. A common feature of these proteins is altered behavior under load, such as exposure of cryptic binding sites (Brown and Discher, 2009) or modified binding kinetics (Kong et al., 2009). An alternative and distinct mechanosensing mechanism, however, has been observed for the FA protein zyxin, which is induced to relocate to SFs under strain, whether through naturally occurring tears (Smith et al., 2011), through optogenetically induced strain (Oakes et al., 2017), or when cells are placed under an externally applied cyclic stress (Hoffman et al., 2012; Yoshigi et al., 2005).

The family of proteins that are characterized by their Lin-11, Isl-1, Mec-3 (LIM) domains, consisting of two zinc fingers, act as important scaffolds for protein-protein interactions (Smith et al., 2014; Sala and Ampe, 2018; Koch et al., 2012; Gill, 1995). Over the last two decades, many LIM domain-containing proteins (LDP), in addition to zyxin, have been identified as mechanoresponsive cytoskeletal elements including paxillin (Smith et al., 2013), Hic-5 and CRP2 (Suzuki et al., 2005). More recently, it has been shown that several LDPs, including members of the zyxin, paxillin, Enigma, and FHL families, share an evolutionarily conserved mechanism by which their LIM domains recognize mechanically strained F-actin (Sun et al., 2020; Winkelman et al., 2020). In all these cases, their tandem LIM domains were necessary and sufficient for this mechanosensitive relocation. Remarkably, however, not all LDPs display mechanosensitive behavior, and the mechanoresponse is not identical amongst LDPs. For instance, both zyxin and paxillin recognize SF strain sites (SFSS), but only zyxin relocates to SFs in response to cyclical stretch (Smith et al., 2013; Suzuki et al., 2005). This implies that LIM domain protein mechanosensitivity is specific and regulated. Dissecting these LDP-specific mechanosensitivity mechanisms and how they are regulated is necessary to better understand the molecular mechanisms underlying cellular mechanoresponse.

To probe this topic further, we investigated the mechanosensitivity of the multimodular LDP testin. Testin is expressed in the majority of tissues and consists of an N-terminal CR (cysteine-rich), central PET (Prickle, Espinas, Testin), and three C-terminal LIM domains (Boëda et al., 2011; Sala et al., 2017a; Tobias et al., 2001). While the exact function of testin remains tricky to identify, reduced expression has been observed in various tumors and cancer cell lines, which, in conjunction with a number of animal studies, suggests a tumor suppressor function (Sarti et al., 2005; Drusco et al., 2005; Zhu et al., 2012; Gu et al., 2014). While testin has primarily been associated with the actin cytoskeleton, a proteomics-based interactome study additionally identified over 100 putative testin binding partners in a domain-specific manner, linking testin to adhesions, microtubules, endocytosis, and nuclear receptor-mediated transcription, among others, illustrating testin's likely multifunctional nature (Sala et al., 2017b). Truncation variants consisting of either the N-terminal CR and PET domains or the C-terminal LIM domains have also been shown to localize to SFs and FAs, respectively (Garvalov et al., 2003; Sala et al., 2017b). In contrast, full-length testin is mainly distributed in the cytoplasm, consistent with its multiconformational nature (Garvalov et al., 2003; Sala et al., 2017a). Together, these findings suggest that the regulation of testin's activity, and thus its mechanosensitivity, is likely mediated by its conformational state. We therefore hypothesized that testin is mechanosensitive under certain conditions and exploited its modular nature to investigate its potential role in recognizing local strain in the actin cytoskeleton.

RESULTS

The LIM domains of testin, but not the full-length protein, recognize stress fiber strain sites

A subset of LIM domain proteins, including members of the FHL, zyxin, and paxillin families, are known to recognize SFSSs via their LIM domains (Smith et al., 2011; Sun et al., 2020; Winkelman et al., 2020). To investigate whether the LIM domains of testin (LIM 1-2-3, Figure 1A) display a similar mechanosensitive behavior, we engineered a series of truncations fused to GFP and coexpressed them with mApple-actin in human foreskin fibroblasts (HFF). LIM 1-2-3 localizes to FAs as previously reported (Figure 1A; Garvalov et al., 2003). We then used a laser photoablation system to locally induce a SFSS, marked by recoil and thinning of the SF (Figure 1B, Smith et al., 2011). Potential recruitment was monitored by tracking the GFP signal over time using a mask based on the brightest pixels in the region surrounding the ablation that increased the most in intensity compared with their preablation state (Figure 1, B and C; Supplemental Figure S1). The same pixels were then used to monitor the intensity of actin in those regions. Following photoablation, we observed a rapid increase in the GFP signal within seconds as LIM 1-2-3 relocated to the induced SFSS and a concomitant loss of actin intensity as the SF was damaged (Figure 1, B and C; Supplemental Movie S1). Following LIM 1-2-3 recruitment, the actin signal subsequently recovered within minutes, indicating SF repair (Smith et al., 2011), before it finally plateaued. To verify that laser-induced damage actually results in the induction of a SFSS, we combined our laser photoablation approach with traction force microscopy and show that the ablated SFs remain under tension while LIM 1-2-3 is recruited (Supplemental Figure S2; Supplemental Movie S2). This suggests that our ablation is likely damaging a subset of filaments in the SF, leaving the remaining intact filaments to bear an elevated force load, which results in increased strain in the remaining filaments.

To assess the spatial distribution of the LIM 1-2-3 localization, we aligned the masks to the angle of ablation, summed each experimental group over time, and averaged them to create a spatial probability map (Supplemental Figure S1D). This map clearly shows that the brightest LIM 1-2-3 signal is located in the center of the mask stack where the ablation occurred (red line, Figure 1C) and where the region of strain is located (dashed circle, Figure 1C). To confirm that this is a SFSS, we assessed relocation of LIM 1-2-3 in the presence of mCherry-conjugated zyxin, a known SF strain sensor (Smith et al., 2011), and used SiR-Actin to visualize the SFs. Masks in these experiments were created based on regions where zyxin increased in intensity. Immediately following strain induction, both zyxin and LIM 1-2-3 relocated to and colocalized at SFs with similar kinetics, confirming that the LIM domains of testin recognize actual SFSSs (Figure 1D; Supplemental Movie S3). Similar results were seen in zyxin-null MEFs (Supplemental Figure S3; Supplemental Movie S4), indicating that relocation of LIM 1-2-3 to SFSSs is independent of zyxin.

In contrast to its LIM domains, full-length (FL) testin is mainly cytoplasmic, with only a small subpopulation localizing to FAs (Figure 1E). When a SFSS was induced, we did not observe recruitment of FL testin (Figure 1, F and G; Supplemental Movie S1) and instead saw a rapid recovery of fluorescence intensity consistent with diffusion. Correspondingly, the spatial probability of recruitment map shows a random distribution and no regions of local enrichment in the central region of strain (Figure 1G). When this experiment was repeated using zyxin as a control, we observed a rapid relocation of zyxin, but not testin, to sites of strain. This confirms that under steady-state conditions FL testin is unable to recognize SFSSs (Figure 1H; Supplemental Movie S3).

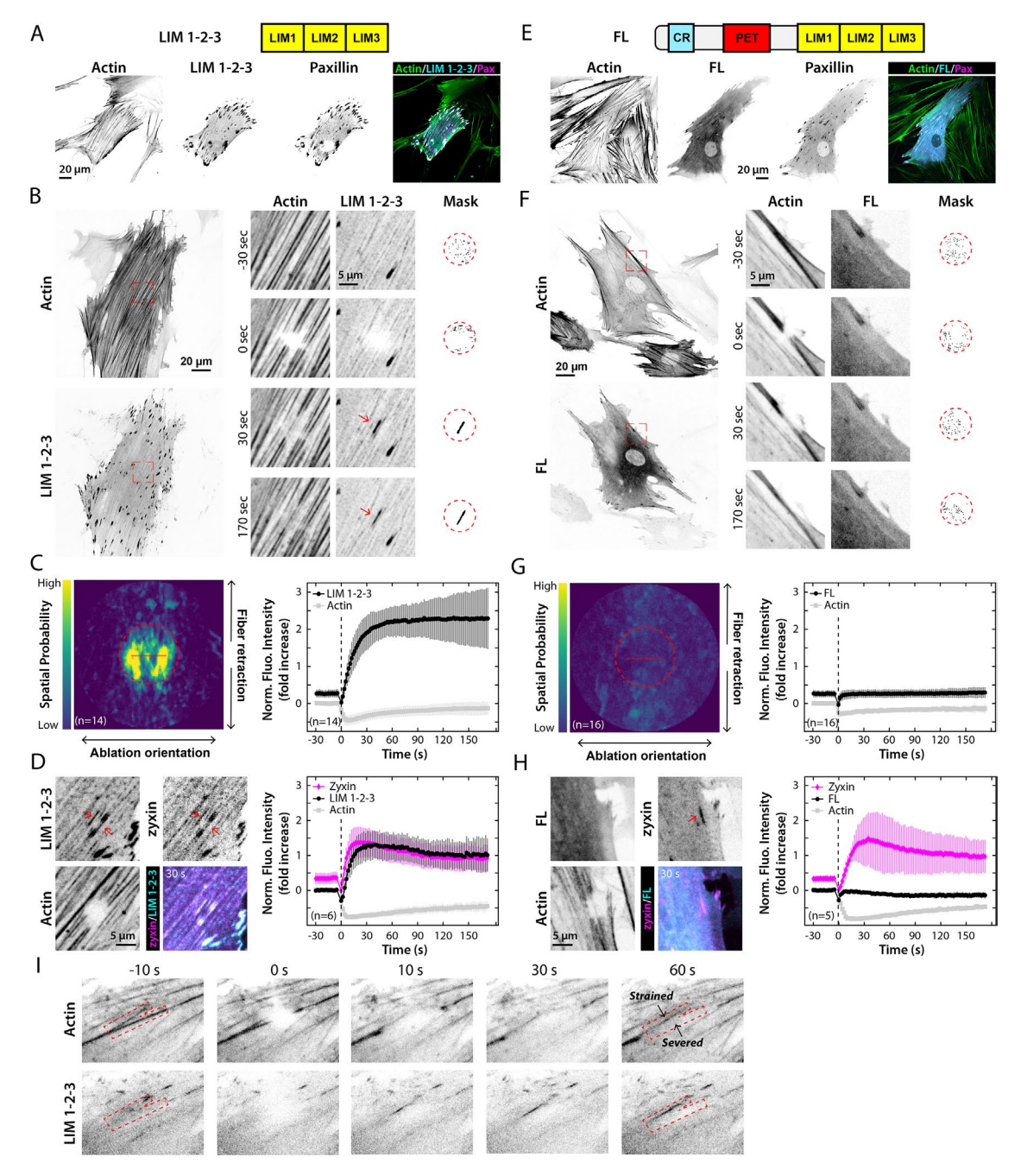


FIGURE 1: The LIM domains of testin, but not full-length, recognize stress fiber strain sites. (A, E) Domain organization and subcellular localization of the LIM domains of testin (LIM 1-2-3) and full-length testin (FL) in HFFs. GFP-LIM 1-2-3 localizes strongly to FAs, A, whereas GFP-FL displays a diffuse cytoplasmic and weak FA localization, E. GFP-testin, mApple-paxillin, and SiR-Actin channels are shown. (B, F) HFFs coexpressing mApple-actin and either GFP-LIM 1-2-3, B, or GFP-FL testin, F. Magnified inset images (red boxed regions) display the localization of each construct during the time lapse. Red arrows indicate relocation of LIM 1-2-3 to SFSSs (Supplemental Movie S1). Masks show the pixels in the region surrounding the ablation (red dashed circle) that increased the most in intensity compared with their preablation state. (C, G) Spatial probability of testin recruitment (left) and average fluorescence intensity traces with SD of the testin and actin signals (right) in the region of strain. The brightest LIM 1-2-3 signal is located in the central region of strain—C, dashed circle—whereas the brightest FL signal is distributed randomly—G. The red line represents the 5-µm laser line used to photoinduce SFSSs. Following SFSS induction, a rapid and large increase of the LIM 1-2-3 signal, C. but no change of the FL testin signal was detected in the region of strain, G. (D, H) Experiments shown in C and G were repeated in the presence of the SFSS marker mCherry-zyxin and SiR-Actin (Supplemental Movie S3). Increased LIM 1-2-3 fluorescence intensity was seen in the region of strain and colocalization with zyxin at SFSSs—D, red arrows. FL signal remained unchanged after ablation and did not colocalize with zyxin—H. (I) HFFs expressing mApple-actin and GFP-LIM 1-2-3 during ablation of Y-shaped SFs are shown (red dashed box). LIM 1-2-3 relocates to the strained SF but not the severed SF (Supplemental Movie S5).

The LIM domains of testin recognize strained, but not severed, stress fibers

Previous work has demonstrated the presence of free barbed ends in naturally occurring spontaneous SFSSs (Smith et al., 2011). This raises the possibility that the LIM domains of testin associate with these barbed ends in SFSSs in addition to recognizing strained actin fibers. To test this, we increased the local laser power to completely sever SF bundles and assessed whether testin's LIM domains recognized free actin filament ends in the absence of strain. Figure 11 shows two SFs arranged in a Y-shape (red box), where the bottom fiber is completely severed, confirmed by the complete loss of the actin signal, and the top fiber becomes strained. Recruitment of LIM 1-2-3 only occurred on the strained fiber, and not along the retracting fiber with the free ends (Figure 11; Supplemental Movie S5). This demonstrates that testin's LIM domains do not recognize barbed actin filament ends.

A single LIM domain is sufficient to recognize stress fiber strain sites

To further dissect the mechanoresponsive regions within testin's LIM domains, we investigated the ability of the individual LIM domains (LIM 1, LIM 2 and LIM 3; Figure 2) to recognize SFSSs. Previous research has suggested that multiple LIM domains are required for mechanosensitivity (Sun et al., 2020; Winkelman et al., 2020). Surprisingly, the LIM1 domain of testin displayed FA localization (Figure 2A) and also relocated to SFSSs (Figure 2, B and C; Movie S6). LIM2 and LIM3, however, were mainly cytoplasmic (Figure 2, D and G) and incapable of recognizing SFSSs (Figure 2, E, F, H, and I). To compare the recruitment magnitude and kinetics to SFSSs of testin's LIM domains, we fitted an exponential recovery curve to the average traces of the various constructs (Figure S4) and calculated the $t_{1/2}$, amplitude, and plateau maximum of the exponential fit (Figure 2L; Supplemental Table S1). Based on these values, the recruitment kinetics of LIM 1-2-3 is very similar to those of the LIM1 domain (Table S1, Figure 2, K and L). These data illustrate that testin's LIM1 domain recognizes SFSSs and that its mechanosensitivity is blocked in the full-length protein.

The N-terminal and C-terminal halves of testin recognize different mechanical states of F-actin

We next tested whether the N-terminal half of testin (NT), containing the CR and PET domains (Figure 3A), is capable of recognizing SFSSs. Despite an initial strong SF localization (Figure 3A), we did not observe any obvious enrichment of NT at SFSSs (Figure 3, B and C; Supplemental Movie S1). However, quantification of the fluorescence intensity in the masked region of strain did reveal a slight increase of the NT signal (Figure 3, D and E). Upon closer examination we noticed that the actin signal simultaneously increased in these regions, opposite to what is expected for a SFSS (Figure 3D). Examination of the spatial distribution of the recruitment revealed that the brightest NT signal was located outside of the central region of strain along the recoil axis of the actin (Figure 3C) and was smaller in magnitude than the LIM 1-2-3 signal (Figure 3E). Together these data indicate that, unlike LIM 1-2-3, the increase in fluorescence of NT arises from a condensation of severed actin filaments and not from additional recruitment (Figure 3, C and D). Therefore, in contrast to its LIM domains, the N-terminal half of testin is unable to bind SFSSs.

To further illustrate this, we coexpressed LIM 1-2-3 and NT and assessed whether the two halves of testin colocalized at all following induction of a SFSS (Figure 3F; Supplemental Movie S7). To ensure full repair of the ablated SF, we monitored their localization over a

time period of 30 min (Figure 3, F and G). Prior to SFSS induction, LIM 1-2-3 localized to FAs, whereas NT localized to SFs as mentioned above (Figure 3, F and G). After SFSS induction, LIM 1-2-3 was immediately recruited to the strain site (arrows, Figure 3, F and G), while NT simultaneously dissociated from the strain region (Figure 3, F and G). NT remained bound to SFs in the regions flanking the strain site. As the SFSS was repaired over time, LIM 1-2-3 dissociated from the ablated SF and NT reassociated with the repaired actin fibers (Figure 3, F and G). The absence of colocalization of NT and LIM 1-2-3 at either SFs or SFSSs demonstrates that the two halves of testin recognize different mechanical states of F-actin.

Tyrosine mutations in the PET and LIM 1 domains drive testin to stress fiber strain sites and focal adhesions

Given the multiconformational nature of testin (Garvalov et al., 2003; Sala et al., 2017a), it is possible that the inability of FL testin to recognize SFSSs results from a conformational state that makes the LIM domains inaccessible. Previous work demonstrated that tyrosine 288 (Y288) in the first LIM domain is structurally important for testin dimerization, because mutating this tyrosine to alanine strongly inhibits dimerization (Sala et al., 2017a). Therefore, we hypothesized that mutating Y288 to alanine would allow testin to recognize strain in the actin cytoskeleton by potentially adopting a more favorable conformation.

To investigate this, we coexpressed a GFP-Y288A mutant of testin (Y288A; Figure 4A) along with actin in HFFs and assessed its ability to relocate to SFSSs (Supplemental Movie S8). Induction of SFSSs resulted in moderate but obvious recruitment of Y288A to the site of strain (Figure 4A). The spatial probability map also revealed a preference for recruitment in the region of strain (Figure 4B). To further investigate the potential regulatory role of Y288 in determining testin's mechanosensitivity, we created phosphomimetic glutamic acid (Y288E) and nonphosphorylatable phenylalanine (Y288F) mutants of testin and assessed their ability to recognize SFSSs (Figure 4, C–F; Supplemental Movie S8). Similarly to Y288A, Y288E was capable of recognizing SFSSs (Figure 4, C, D, G, and H). Conversely, the Y288F mutant did not display this mechanosensitive behavior (Figure 4, E–H). These data illustrate that specific mutations of Y288 in the first LIM domain can promote testin's mechanosensitivity.

The observation that Y288A/E mutations drive testin to SFSSs implies the accessibility of the LIM domains is enhanced in these mutants. Because the truncated LIM domains of testin, but not FL testin, strongly localize to FAs (Figure 1, A and E), we hypothesized that the mechanosensitive Y288A/E mutants would display increased FA localization. To investigate this, we coexpressed either Y288A or Y288E with paxillin, another FA protein, and assessed their FA localization (Figure 4I). To quantify FA localization, we calculated the ratio of the fluorescence intensity in FAs and the cytoplasmic region surrounding the FAs for every FA in a given cell (Figure 4J; Supplemental Figure S5). In agreement with the results obtained from the laser photoablation assay, we found that FA localization of the mechanosensitive Y288A/E mutants was significantly increased compared with the nonmechanosensitive Y288F mutant (Figure 4J). The Y288F mutant displayed FA localization that was comparable to that of the WT protein (Figure 4J), which is consistent with their inability to recognize sites of SF strain.

Testin forms dimers through interactions involving its PET domain and its first two LIM domains (Sala et al., 2017a). Because specific mutations of Y288, located in the dimerization region of the protein, promote testin's mechanosensitivity, we reasoned that other tyrosines in those dimerization regions might similarly affect its

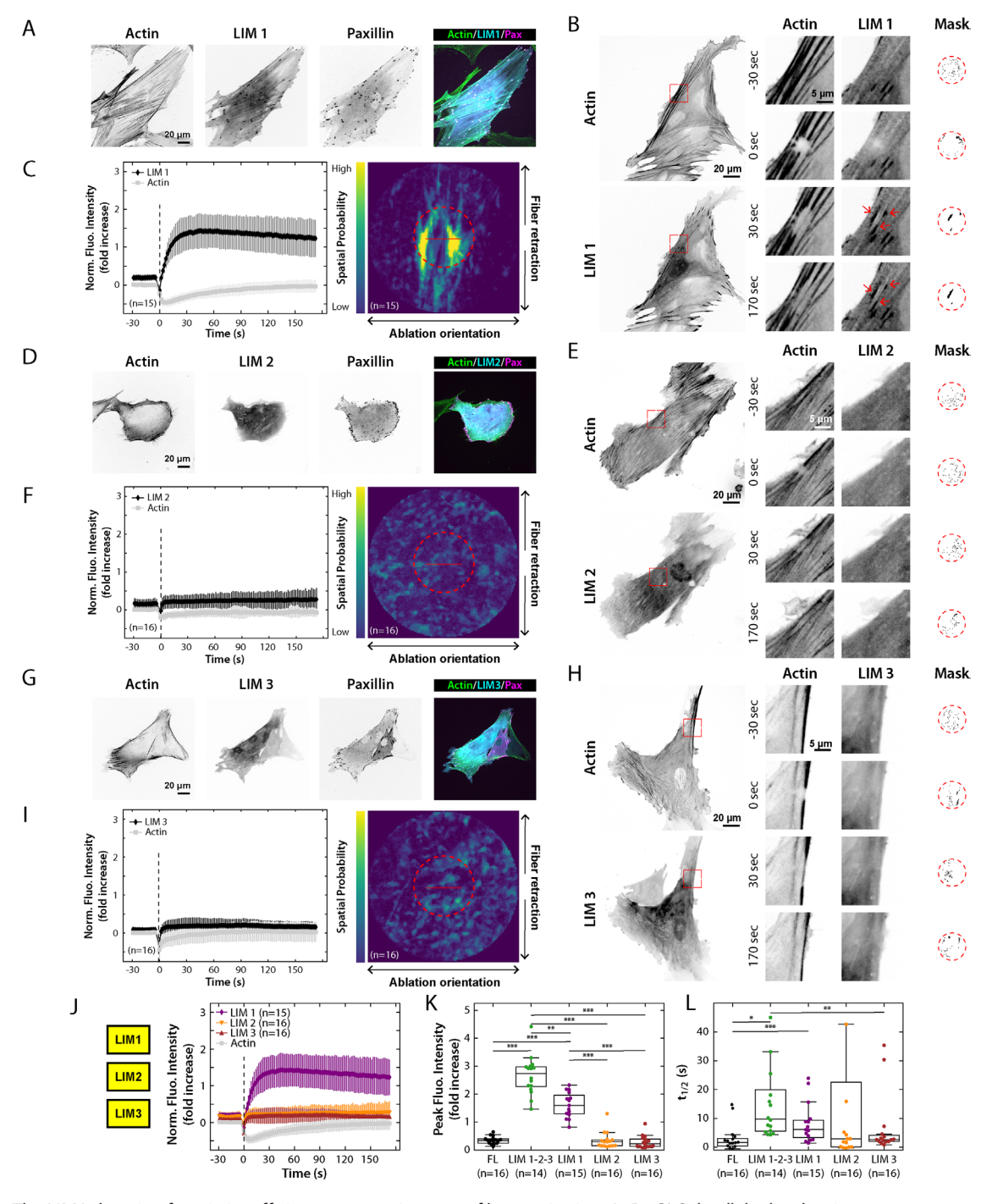


FIGURE 2: The LIM1 domain of testin is sufficient to recognize stress fiber strain sites A, D, G) Subcellular localization of the individual LIM domains of testin in HFFs. Only the LIM1 domain localizes to FAs. GFP-testin, mApple-paxillin, and SiR-Actin channels are shown. (B, E, H) HFFs expressing mApple-actin and GFP-LIM 1, B; GFP-LIM 2, E; or GFP-LIM 3, H. Magnified inset images (red boxed regions) display the localization of each construct during the time lapse, demonstrating relocation to SFSSs of only LIM1 (red arrows, Supplemental Movie S6). Mask images show the pixels in the region surrounding the ablation (red dashed circle) that increased the most in intensity compared with their preablation state. (C, F, I) Average fluorescence intensity traces and SD of the LIM and actin signals (left) and spatial probability of LIM recruitment (right) in the region of strain. Following SFSS induction, a rapid and large increase of only LIM1 was detected in the region of strain (left) and the brightest LIM1 intensity was located in the central region of strain (right, dashed circles). Red line represents the 5- μ m laser line used to photo-induce SFSSs. (J) Average fluorescence intensity traces and SD of testin's individual GFP-coupled LIM domains and mApple-actin signals in the region of strain indicating recruitment to SFSSs of only LIM1. (K) Distribution of the peak fluorescence intensities after SFSS induction per testin variant. (L) Recruitment $T_{1/2}$ after SFSS induction per testin variant. * $p \le 0.05$, *** $p \le 0.01$, *** $p \le 0.001$. Dashed vertical lines in C, F, I, and J indicate the ablation timepoint.

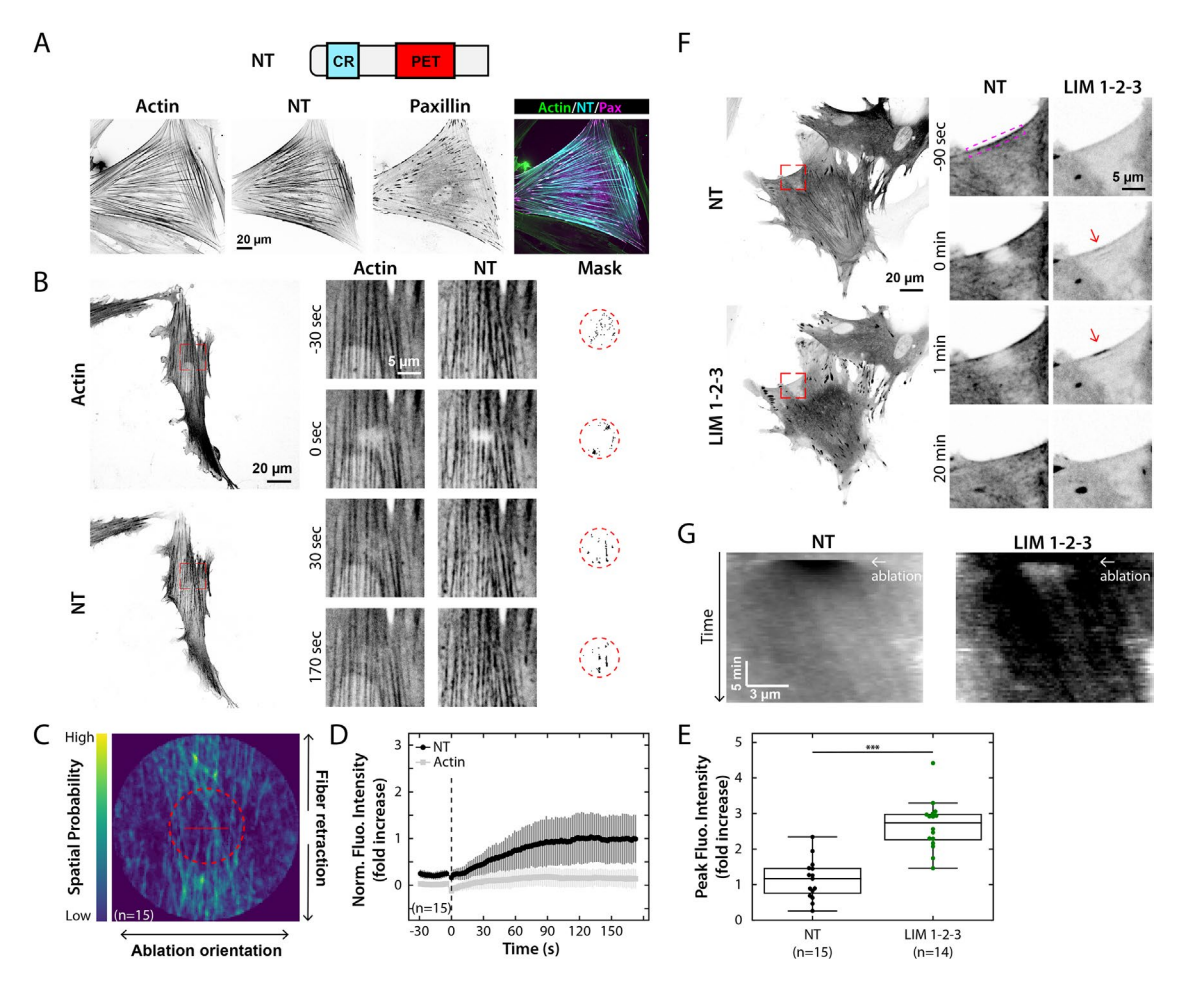


FIGURE 3: The N-terminal domains and C-terminal LIM domains of testin recognize different mechanical states of SFs. (A) Domain composition and subcellular localization of the N-terminal domains of testin (NT). GFP-NT localizes strongly to SFs. GFP-NT, mApple-paxillin, and SiR-Actin channels are shown. (B) HFFs coexpressing mApple-actin and GFP-NT. Magnified inset images (red boxed regions) display the localization of NT during the time lapse (Supplemental Movie S1). Masks show the pixels in the region surrounding the ablation (red dashed circle) that increased the most in intensity compared with their preablation state. (C) Spatial probability of NT recruitment in the region of strain shows that NT is primarily recruited outside the central region of strain (red dashed circle). Red line represents the 5- μ m laser line used to photoinduce SFSSs. (D) Average fluorescence intensity trace and SD of the NT and actin signals in the region of strain. Dashed vertical line indicates the ablation time point. (E) Distribution of the peak fluorescence intensities after SFSS induction for NT and LIM 1-2-3. **** $p \le 0.001$. (F) HFFs coexpressing GFP-LIM 1-2-3 and mApple-NT. Magnified inset images (red boxed regions) display the localization of each construct during time lapse showing recruitment of GFP-LIM 1-2-3 to SFSSs (red arrows) and absence of colocalization of GFP-LIM 1-2-3 and mApple-NT (Supplemental Movie S7). (G) Kymograph along the magenta boxed SF in F showing recruitment of LIM-1-2-3 to the SFSS following ablation and simultaneous dissociation of NT in the same region. Arrows indicate the ablation timepoint.

mechanosensitivity. We therefore investigated tyrosine 111 (Y111), located in the PET domain, by creating nonphosphorylatable alanine (Y111A) and phenylalanine (Y111F) mutants as well as a phosphomimetic glutamic acid (Y111E) mutant (Figure 5, A–F; Supplemental Movie S8). Interestingly, we observed similar behavior for the Y111 mutants with clear recruitment of Y111A (Figure 5, A, B, G, and H) and Y111E (Figure 5, C, D, G, and H) mutants to SFSSs but not the Y111F mutant (Figure 5, E–H). In agreement with the results from the Y288 mutants, FA localization of the mechanosensitive Y111A/E mutants was significantly increased compared with that of the nonmechanosensitive Y288F mutant (Figure 5J). Our quantitative analysis further revealed that FA localization (Figure 5J) of the Y111A and Y111E mutants, as well as their relocation to sites of SF strain (Figure 5, G and H), was stronger than what we observed for the corresponding mechanosensitive Y288 mutants (Figure 4, G, H,

and J), suggesting these mutants recognize FAs and SFSSs with different affinities (Supplemental Figure S4; Supplemental Table S1). Together, these results demonstrate that mutations in the dimerization regions of testin affect its ability to recognize strain in the actin cytoskeleton, and that the magnitude of the effect is dependent on the nature of the mutation.

Activated RhoA promotes SF localization of testin

The behavior of the various truncations and tyrosine mutants in comparison with that of WT FL testin implies that its mechanosensitivity must be regulated. Because local strain induction at SFs is not sufficient for testin to recognize these sites, we hypothesized that perturbing upstream signaling regulating the actin cytoskeleton at the cellular scale might promote testin's mechanosensitivity. Because RhoA is known to modulate the overall cellular contractility and actin

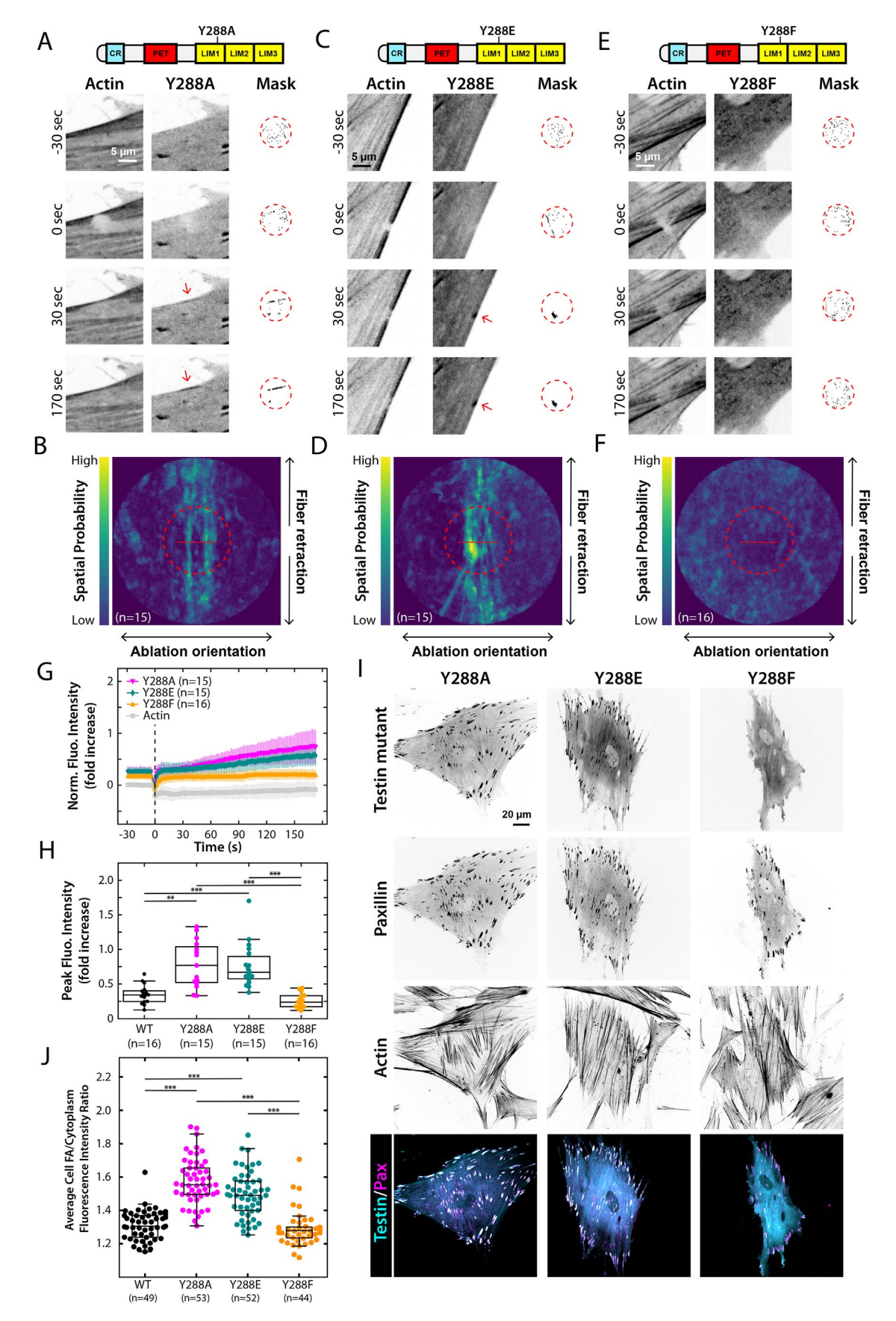


FIGURE 4: The Y288A and Y288E mutants of testin recognize SFSSs. (A, C, E) HFFs coexpressing mApple-actin and either GFP-Y288A, A; GFP-Y288E, C; or GFP-Y288F, E. Magnified inset images (red boxed regions) display the localization of each construct during the time lapse demonstrating relocation to SFSSs of both the Y288A and Y288E

cytoskeleton organization (Ridley and Hall, 1992; Oakes et al., 2017), we transfected cells with mApple-conjugated FL testin in conjunction with either a constitutively active RhoA (CA-RhoA) or dominant negative RhoA (DN-RhoA) variant and assessed the localization of testin under different levels of cytoskeletal tension (Figure 6A). Cells expressing the CA-RhoA variant were more contractile (Figure 6B), and 90% of these cells exhibited SF localization of testin (Figure 6, A and C), compared with 26% of the control cells, where testin was primarily cytoplasmic (Figure 6, A and C). Correspondingly, in only 17% of the DN-RhoA expressing cells, testin localized to SFs and was mainly distributed in the cytoplasm (Figure 6, A and C).

To investigate whether increased SF localization of testin is driven by RhoA or merely the effect of increased cellular contractility and tension, we monitored testin localization in cells treated with the drug calyculin A to increase cellular contractility without stimulating RhoA activity (Chartier et al., 1991; Lemmon et al., 2009; Stricker et al., 2011). Traction force microscopy analysis demonstrates that the cells become more contractile after calyculin A treatment (Figure 6D). Testin localization, however, remained unaffected (n = 14 cells examined), illustrating that increased cellular contractility is not sufficient to drive the protein to SFs and that upstream RhoA signaling is required for testin relocation to SFs (Figure 6, A–D).

Given that activated RhoA affects testin localization, we next examined whether elevated RhoA activity also enables testin to recognize SF strain. To test this, we repeated our laser photoablation experiment with FL testin in cells expressing CA-RhoA (Figure 6, E and F; Supplemental Movie S9). In contrast to the control cells (Figure 1, F and G), we saw recruitment of FL testin to the site of strain (Figure 6E) and an increase in fluorescence intensity of testin over time that corresponded with a simultaneous decrease in the actin intensity in those regions (Figure 6F). Combined, these results indicate that elevated RhoA activity promotes testin's SF localization and mechanosensitivity.

DISCUSSION

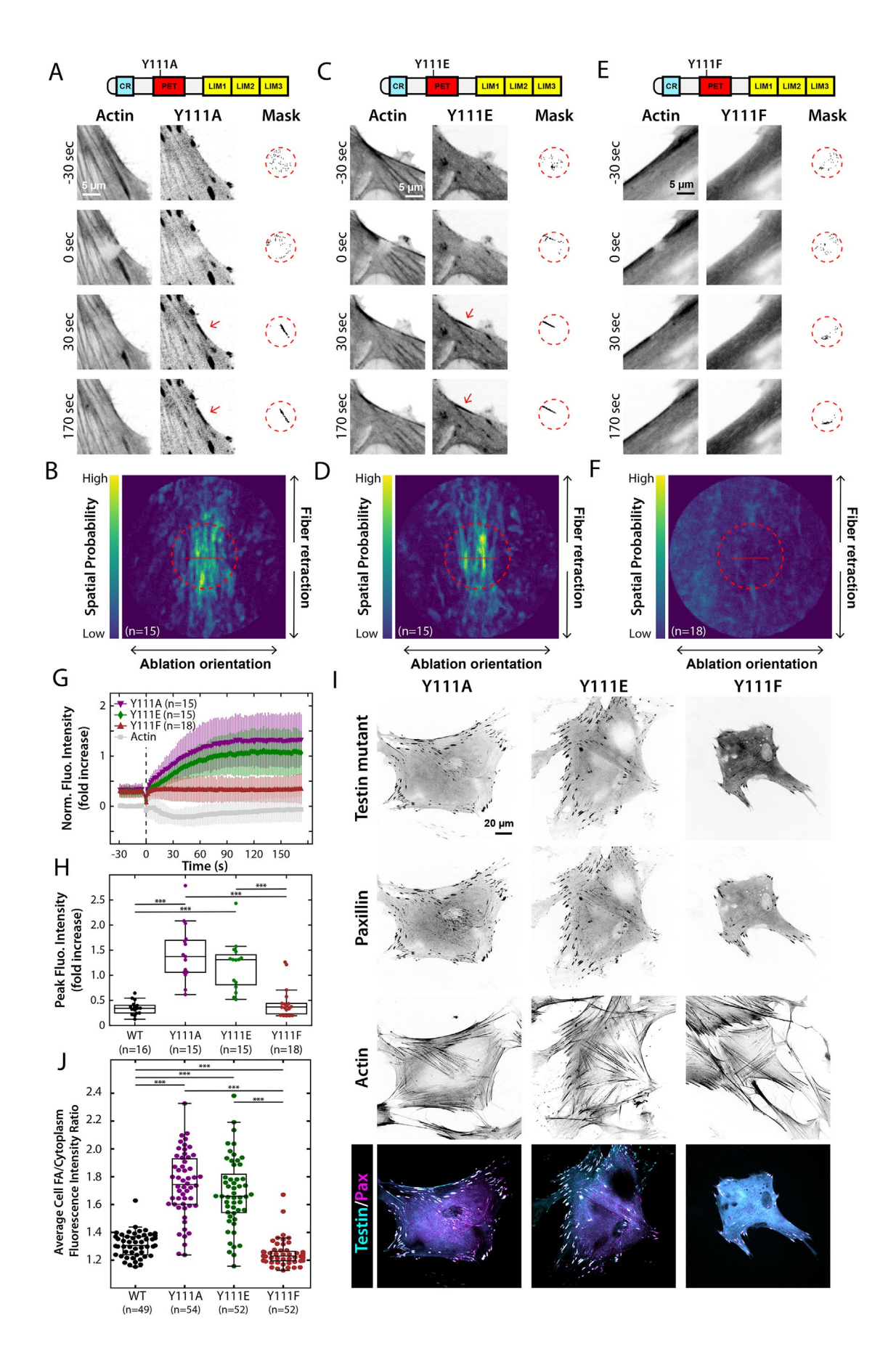
Our data reveal that the mechanosensitivity of the LDP testin is highly regulated, likely through modification of its biochemical and/ or conformational state, potentially allowing cells to control its spatiotemporal behavior through signaling molecules such as RhoA. Over the last decade, it has become more apparent that the mechanical state of filamentous actin (tension, curvature, torsion) affects the binding and activity of many actin-binding proteins (Jégou and Romet-Lemonne, 2021; Zimmermann et al., 2017). Recent work (Sun et al., 2020; Winkelman et al., 2020) has suggested that a conserved mechanism in LIM domains confers mechanosensitivity to strained actin filaments on proteins from the FHL, zyxin, and paxillin families, among others. The LDP testin appears unique in that the FL

protein resides primarily in the cytoplasm, while its N-terminal half recognizes SFs and its C-terminal half recognizes SFSs and FAs (Figures 1–3). Although the functional consequences of this unique feature are currently unknown, we speculate that testin acts as a bifunctional scaffold protein in mechanically stressed actin-rich structures.

Recent works comparing LDPs have shown that there exists a large diversity in their LIM domain sequences and have suggested that multiple successive LIM domains are required to recognize SFSSs (Sun et al., 2020; Winkelman et al., 2020). We show, however, that the LIM1 domain of testin can recognize SFSSs on its own in cells (Figure 2). This discrepancy between testin and other LDPs is likely due to differences in the sequence of testin's LIM domains. Sun et al. (2020) have proposed that a conserved phenylalanine in LIM domains is vital for their mechanosensitivity, but only one of testin's LIM domains (LIM 3) contains this amino acid in the conserved place (Sala et al., 2017a). This seeming contradiction could have a number of potential explanations. First, and most excitingly, different LDPs could use different mechanisms to recognize SFSSs. Alternatively, the relative amount of strain in the actin filaments could differentially affect their conformation and hence the ability of a LIM domain to associate with them. In other words, the strain we induce in actin filaments using a laser might be slightly different from the strain induced through natural tears and ruptures. Lastly, we cannot rule out that testin's LIM1 domain is indirectly associating with strained actin via recruitment by other SFSS proteins, or by interacting with endogenous testin in such a manner to activate its inherent mechanosensitivity. The LIM domains of testin have been shown to interact with zyxin, VASP and alpha-actinin (Garvalov et al., 2003; Sala et al., 2017b), which are all found in SFSSs (Smith et al., 2011). This last scenario, however, seems unlikely since we find that LIM 1-2-3 recruitment to SFSSs is independent of zyxin (Figure S3) and, more importantly, that the recruitment kinetics of the LIM1 domain of testin is comparable to the recruitment kinetics of LIM 1-2-3 (Figure S4). Ultimately, in vitro and structural studies of individual LIM domains bound to strained actin will likely be necessary to elucidate the exact mechanisms. Finally, the differences in magnitude of SFSS recognition of the individual LIM1 domain and the LIM 1-2-3 variant are likely a result of an additive contribution, as suggested previously for zyxin's LIM domains (Winkelman et al., 2020).

While the N-terminal half of testin clearly localizes to SFs, our data illustrate that it is not mechanosensitive on its own (Figure 3). We hypothesize that it might play a role in maintaining SF homeostasis in conjunction with the LIM domains. Certain actin-binding proteins have indeed been shown to form cocomplexes with either the LIM domains (e.g., Ena/VASP proteins; Garvalov et al., 2003; Boëda et al., 2007; Sala et al., 2017b) or N-terminal domains (e.g., calponin-2; Sala et al., 2017b) of testin, showing that both halves

mutants—A and C, red arrows—but not the Y288F mutant—E (Supplemental Movie S8). Masks show the pixels in the region surrounding the ablation (red dashed circle) that increased the most in intensity compared with their preablation state. (B, D, F) Spatial probability of recruitment of the Y288 testin mutants in the region of strain. The brightest Y288A and Y288E signals are located in the central region of strain—B and D, dashed circles—whereas the brightest Y288F signal is distributed randomly—F. Red lines represent the 5- μ m laser line used to photoinduce SFSSs. (G) Average fluorescence intensity traces and SD of the Y288 testin mutants and actin signals in the region of strain indicating recruitment of the Y288A and Y288E mutants, but not the Y288F mutant, to SFSSs. Dashed vertical line indicates the ablation timepoint. (H) Distribution of the peak fluorescence intensities after SFSS induction for WT testin and the Y288 mutants. ** $p \le 0.01$, *** $p \le 0.001$. (I) Subcellular localization in HFFs of the Y288 mutants. The mechanosensitive Y288A and Y288E mutants strongly localize to FAs whereas the nonmechanosensitive Y288F mutant displays diffuse cytoplasmic localization and only weak FA localization. GFP-testin, mApple-paxillin, and SiR-Actin channels are shown. (J) Distribution of the average cellular FA/cytoplasmic fluorescence intensity ratio per testin variant. **** $p \le 0.001$.



could contribute to the recruitment of these proteins. Future studies will be needed to investigate the potential function of testin in maintaining the mechanical integrity of SFs.

The numerous point mutations that confer mechanosensitivity on testin suggest that this function of the protein can be regulated. High-throughput mass-spec analyses provide evidence that Y288 and Y111, both located in the dimerization regions of the protein (Sala et al., 2017a), can be phosphorylated (www.phosphosite.org), and phosphomimetic mutations of these tyrosines to glutamic acid (E) make testin mechanosensitive. Interestingly, we found that the alanine (A) mutants are also mechanosensitive, while the phenylalanine (F) mutants are not. These data suggest that the loss of the aromatic ring in the E and A mutants impacts dimerization and frees the mechanosensitive LIM domains to recognize SFSSs. This does not entirely rule out phosphorylation as a mechanism, since phosphorylation has been shown to affect the ability of tyrosines to engage in aromatic stacking interactions, thereby impacting proteins' local structure and function (Feng et al., 2010; Nishi et al., 2011). It is thus possible that phosphorylation of Y288 or Y111 similarly alters testin's conformation and hence mechanosensitivity. The differences in kinetics we see between mutations at positions Y288 and Y111 are likely related to their local effect on the conformation of the protein and its associated potential impact on dimerization. Structural studies, however, will be necessary to confirm and elucidate these underlying mechanisms. It is, however, remarkable that all the mechanosensitive variants of testin showed increased localization to FAs. This is consistent with our previous observation that the regions where SFs are coupled to FAs likely contain sites of strained actin filaments (Oakes et al., 2017), though it does not preclude the possibility that testin could be binding other FA proteins. A similar tension-dependent recruitment of testin to focal adherens junctions has been observed in endothelial cells, raising the possibility that testin plays an analogous role in cell-cell junctions (Oldenburg et al., 2015).

Our data also indicate that activation of RhoA causes WT testin to relocate to SFs and recognize SFSSs (Figure 6). This suggests that signaling proteins downstream of RhoA potentially affect testin's biochemical and/or conformational state, thereby changing its mechanosensitive behavior as well. Although our data do not exclude the possibility that SF localization of testin in the presence of CA RhoA is partially mediated by its N-terminal domains, our laser ablation analysis demonstrates that the recognition of a SFSS by FL testin under these conditions is mediated by its LIM domains (Figure 6F). Specifically, the increase in actin signal in Figure 3D

following ablation indicates that the N-terminal domains are unable to recognize SFSSs and merely colocalize with condensing actin in the regions adjacent to the strain. In contrast, the loss of actin intensity following ablation in Figure 6F is indicative of the induction of a SFSSs (Smith et al., 2011, 2013) and similar to the actin traces we observed for all the other mechanosensitive testin variants in this study. Together, these demonstrate that SFSS recognition by FL testin in the presence of activated RhoA is mediated by its LIM domains. While previous reports have established that many downstream effectors of RhoA, including kinases, show increased activity in response to mechanical forces (Lessey et al., 2012; Torsoni et al., 2005), the precise underlying mechanisms of how RhoA activation modulates testin's mechanosensitivity remain to be explored.

Together, our results imply that testin is only associated with strained SFs under certain conditions, and thus we propose that its mechanosensitivity is actively regulated by the cell. Furthermore, our findings raise the possibility that similar regulatory mechanisms apply to other LDPs, of which only a subset have been identified as mechanosensitive. For example, LIMD1, in contrast to its LIM domains, is incapable of recognizing tensed SFs (Sun et al., 2020), suggesting that its mechanosensitivity is likely also context-dependent. These insights may also help clarify the functional role of testin in cells. Testin is known to affect actin-driven mechanical processes, including cell spreading, cell migration, and proliferation (Griffith et al., 2004; Li et al., 2016; Sala et al., 2017b). Connecting testin's mechanosensitivity to RhoA activity provides important context for interpreting testin's role in these and other cellular processes. Future research will be needed to assess how regulation or dysregulation of testin's mechanosensitivity affects the many cellular functions and diseases in which it is implicated. It remains clear, however, that regulation of LDPs represent an intriguing and broad mechanism for cells to control mechanotransduction activity.

MATERIALS AND METHODS

Request a protocol through Bio-protocol.

Mammalian expression vectors and cloning

For expression as GFP-fusion proteins, cDNAs encoding full-length (FL) testin (amino acids 1–421), full-length Y288A (Y288A substitution), NT (CR and PET domains, amino acids 1-233), LIM 1-2-3 (amino acids 231–421), LIM 1 (amino acids 234–299), LIM 2 (amino acids 299–354), and LIM 3 (amino acids 361–421) were cloned into the multiple cloning site of pEGFP-N3 or pEGFP-C3 (Clontech) as

FIGURE 5: The Y111A and Y111E mutants of testin recognize SFSSs. (A, C, E) HFFs coexpressing mApple-actin and either GFP-Y111A, A, GFP-Y111E, C, or GFP-Y111F, E. Magnified inset images (red boxed regions) display the localization of each construct during the time lapse demonstrating relocation to SFSSs of both the Y111A and Y111E mutants—A and C, red arrows—but not the Y111F mutant—E (Supplemental Movie S8). Masks show the pixels in the region surrounding the ablation (red dashed circle) that increased the most in intensity compared with their preablation state. (B, D, F) Spatial probability of recruitment of the Y111 testin mutants in the region of strain. The brightest Y111A and Y111E signals are located in the central region of strain—B and D, dashed circles—whereas the brightest Y111F signal is distributed randomly—F. Red lines represent the 5- μ m laser line used to photoinduce SFSSs. (G) Average fluorescence intensity traces and SD of the Y111 testin mutants and actin signals in the region of strain indicating recruitment of the Y111A and Y111E mutants, but not the Y111F mutant, to SFSSs. Dashed vertical line indicates the ablation timepoint. (H) Distribution of the peak fluorescence intensities after SFSS induction for WT testin and the Y111 mutants. **** $p \le 0.001$. (I) Subcellular localization in HFFs of the Y111 mutants. The mechanosensitive Y111A and Y111E mutants strongly localize to FAs whereas the nonmechanosensitive Y111F mutant displays a diffuse cytoplasmic localization and only weak FA localization. GFP-testin, mApple-paxillin, and SiR-Actin channels are shown. (J) Distribution of the average cellular FA/cytoplasmic fluorescence intensity ratio per testin variant. **** $p \le 0.001$.

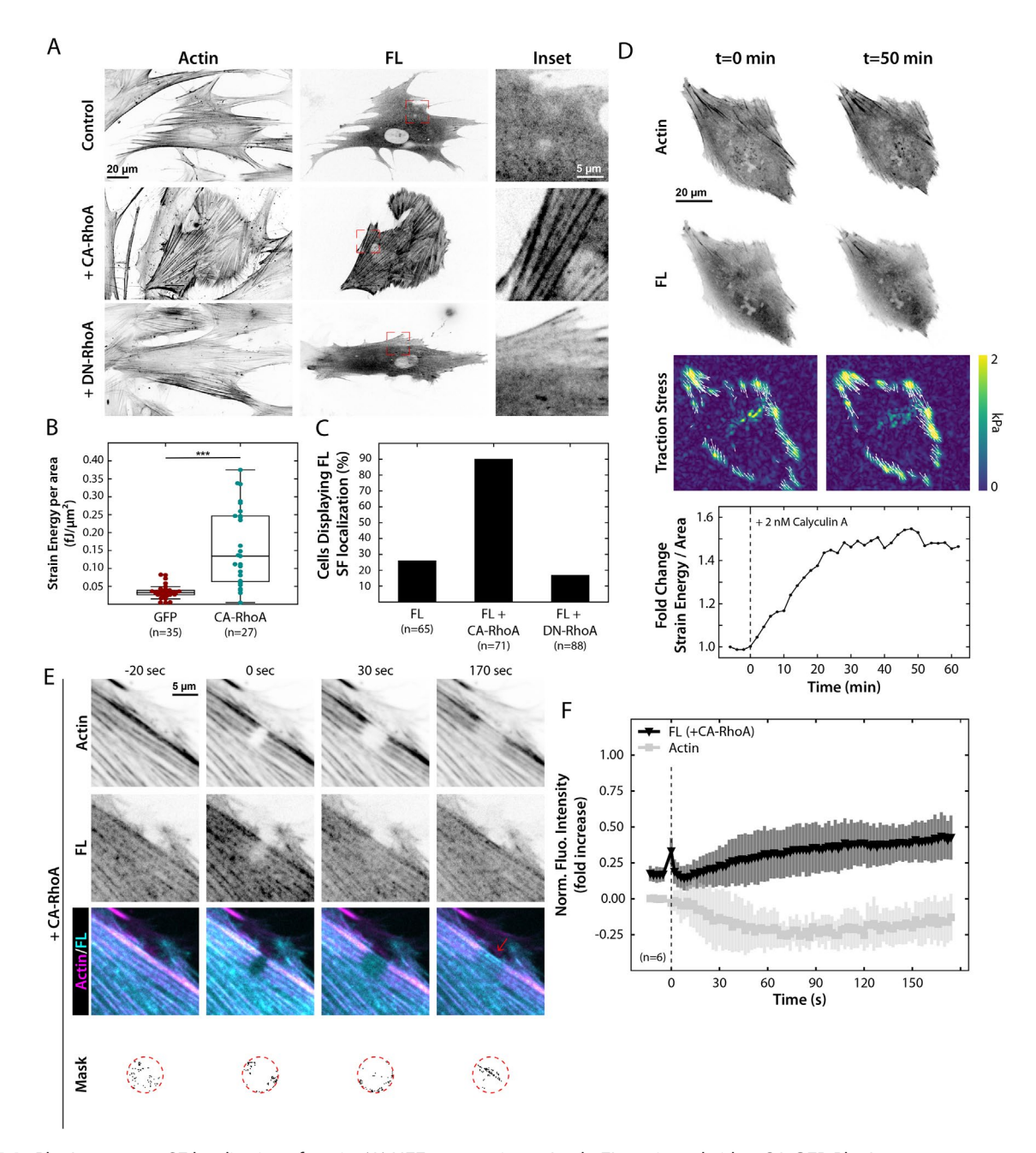


FIGURE 6: RhoA promotes SF localization of testin. (A) HFFs expressing mApple-FL testin and either CA GFP-RhoA or DN GFP-RhoA. In the presence of CA GFP-RhoA, mApple-FL testin relocates to SFs (magnified insets). (B) Measurement of strain energy per area is shown for both the control (GFP) and CA-RhoA expressing cells. In the presence of CA-RhoA, the overall contractility of the cell is increased. *** $p \le 0.001$. (C) Percentage of HFFs displaying SF localization of mApple-FL testin in the absence or presence of either CA-RhoA or DN-RhoA. (D) Representative images of HFFs expressing GFP-actin and mApple-FL testin and their corresponding traction stresses before and after addition of 2 nM Calyculin A. Traction stress vectors (white arrows) are only shown for regions greater than 500 Pa. Calyculin A increases cellular contractility (vertical dashed line) as indicated by the increase in traction stresses and relative change in strain energy per area. (E) HFFs coexpressing mApple-FL testin and CA GFP-RhoA during an ablation. SFs were stained with SiR-Actin. Following strain induction, FL testin relocated to SFSSs (red arrow, Supplemental Movie S9). (F) Average fluorescence intensity traces and SD of FL testin and actin in the region of strain indicating recruitment of FL testin to SFSSs. Dashed vertical line indicates the ablation timepoint.

previously described (Sala et al., 2017a, b). For expression as mApple-fusion proteins, cDNAs encoding full-length testin (amino acids 1–421) and NT (amino acids 1–233) were amplified from the full-length testin pEGFP-N3 vector (Forward primer: 5'-CCGCTCGAGCTATGGACCTG-3', Reverse primer FL: 5'-CGGGATCCCTAAGACATCCTCTTC-3', Reverse primer NT: 5'-CGGGATCCCTATTGA-

GTTCTTTGTGCTC-3') and cloned into the mApple-C1 vector (Addgene plasmid # 54631) using the Xhol and BamHI restriction sites. The Y111E substitution was introduced into the full-length testin pEGFP-N3 vector (Forward primer Y111E: 5'- TACAGTTACC-GAAGAGTGGGCTC-3', Reverse primer Y111E: 5'-TTGATGGAGA-CATTCTTC-3') using the Q5 site-directed mutagenesis kit (E0554S,

New England Biolabs) to generate a point mutant. Y111A, Y111F, Y288E, and Y288F point mutants of GFP-fused full-length testin were a kind gift of Evelyne Friederich and Elisabeth Schaffner-Reckinger (University of Luxembourg, Luxembourg). mCherry-zyxin was a kind gift of Mary Beckerle's laboratory (University of Utah, Salt Lake City, UT). pcDNA3-EGFP-RhoA-T19N (Addgene plasmid #12967) and pcDNA3-EGFP-RhoA-Q63L (Addgene plasmid #12968) were kind gifts from Gary Bokoch. mApple-C1 (Addgene plasmid #4631), mApple-actin (Addgene plasmid #54935), and GFP-actin (Addgene plasmid #54921) vectors were a kind gift from Michael Davidson. All constructs were verified by sequencing.

Cell culture and transfection

Human foreskin fibroblasts (HFF) were obtained from ATCC (CRL-252). Mouse embryonic fibroblasts (MEF) and zyxin^(-/-) MEFs were a kind gift of Mary Beckerle's laboratory (University of Utah, Salt Lake City, UT). HFFs and MEFs were cultured in DMEM (MT10013CV, Corning) supplemented with 10% fetal bovine serum (MT35-010-CV, Corning) and 1% antibiotic–antimycotic solution (MT30004Cl, Corning) at 37°C and 5% CO₂. At 24 h before each experiment, HFFs were transfected with 5 μg total DNA using a Neon electroporation system (ThermoFisher Scientific) and plated on polyacrylamide gels (traction force microscopy) or glass coverslips (laser photoablation, quantification of focal adhesion localization). At 48 h before laser photoablation, zyxin^(-/-) MEFs were transfected with 5 μg total DNA using the Fugene 6 transfection reagent (E2691, Promega) and plated on glass coverslips.

Live cell imaging

Cells were imaged in culture media supplemented with 20 mM HEPES (SH3023701, HyClone) at 37°C, with or without 1 µM SiR-Actin (CY-SC001, Cytoskeleton) or 2 nM Calyculin A (101932-71-2, Cayman), on a Marianas Imaging System (Intelligent Imaging Innovations) consisting of an Axio Observer 7 inverted microscope (Zeiss) attached to a W1 Confocal Spinning Disk (Yokogawa) with Mesa field flattening (Intelligent Imaging Innovations), a Phasor photomanipulation unit (Intelligent Imaging Innovations), a motorized X,Y stage (ASI), and a Prime 95B sCMOS (Photometrics) camera. Illumination was provided by a TTL triggered multifiber laser launch (Intelligent Imaging Innovations) consisting of 405, 488, 561, and 637 lasers, using a 63 × 1.4 NA Plan-Apochromat objective (Zeiss). Temperature and humidity were maintained using a Bold Line full enclosure incubator (Oko Labs). The microscope was controlled using Slidebook 6 Software (Intelligent Imaging Innovations).

Laser photoablation and quantitative analysis of stress fiber strain site recruitment

Prior to initiation of a time lapse, a 5-µm linear region was drawn in Slidebook over the SFs that were to be damaged. Cells were imaged for 3 min and 30 s, alternating between the actin and testin channels, with images taken approximately every 2 s. After 30 s of imaging the steady state, the marked 5-µm region was illuminated with the 405 laser at a power of 370 µW for 1.5 s to induce a SFSS via photoablation. The remainder of the time lapse was then imaged.

Images were analyzed in Python following a scheme laid out graphically in Supplemental Figure S1A. Each time lapse was first broken into two stacks representing the testin channel and the actin channel. Each stack was first flat-field corrected and photobleach corrected (Payne-Tobin Jost and Waters, 2019). The testin channel

was then registered using the whole image via an efficient sub-pixel registration algorithm (Guizar-sicairos et al., 2008). The calculated registration shifts from the testin channel were then applied to the actin channel, and both channels were cropped to a region of 121 × 121 pixels (~21 × 21 µm) centered on the ablation region. For each channel, an average intensity image was created by averaging the frames in the stack before the ablation event. A relative difference was determined at each time point by subtracting the reference image from a given frame, and then dividing by the reference image. A mask of the brightest 5% of points relative to the reference image in the testin channel was created for each time point. The average value of the masked points in each channel was then plotted as a function of time to create a trace of the normalized fluorescence intensity for each movie.

Average traces were created by averaging the traces from mul-

tiple movies and plotting the mean \pm the standard deviation for each time point. To calculate the $t_{1/2}$ value, the average trace curve starting from t=0 was fitted to the equation $I(t)=A-Be^{(-t/k)}$, where $t_{1/2}=\ln\frac{A}{2B}\times -k$. Fits are shown in Supplemental Figure S4 and calculated fit parameters for each testin construct can be found

in Supplemental Table S1.

The offset seen in the testin channel signal trace (e.g., Figure 1C) is a product of making a mask of the 5% of pixels that are brightest compared with the reference image. Because the location of the strain site is dependent on the local architecture of the actin cytoskeleton, we could not simply choose a predetermined region of interest to measure recruitment. By using the pixels that increased in intensity the most relative to the reference image, we were able to create dynamic masks that could identify recruitment independent of the location within the ablation region. Supplemental Figure S1, B and C shows how that offset changes as the number of pixels used in the mask is increased. The trace in the actin channel does not show such an offset because the masked pixels were chosen based on the testin image. For the traces in the control experiments using zyxin (Figure 1, D and H), the masked points were chosen using the zyxin channel and then applied to the testin and actin channels.

To create the spatial probability maps, we took the masks for a given movie and summed them across the entire stack (Supplemental Figure S1D). The resulting image was then rotated to align the direction of the ablation horizontally and then averaged across all the movies for a given condition. The following numbers of ablations were performed for each condition: FL—16; LIM 1-2-3—14; LIM 1—15; LIM 2—16; LIM 3—16; NT—15; Y111A—15; Y111E—15; Y111F—18; Y288A—15; Y288E—15; Y288F—16; FL + CA RhoA—6; Zyxin + LIM 1-2-3—6; Zyxin + FL—5; Zyxin (-/-) + LIM 1-2-3—6.

Traction force microscopy and analysis

Traction force microscopy was performed as described previously (Sabass et al., 2008; Oakes et al., 2017). Coverslips were prepared by incubating with a 2% solution of 3-aminopropyltrimethyoxysilane (313255000, Acros Organics) diluted in isopropanol, followed by fixation in 1% glutaraldehyde (16360, Electron Microscopy Sciences) in ddH₂0. Polyacrylamide gels (shear modulus: 16 kPa—final concentrations of 12% acrylamide [1610140, Bio-Rad] and 0.15% bisacrylamide [1610142, Bio-Rad]) were embedded with 0.04-µm fluorescent microspheres (F8789, Invitrogen) and polymerized on activated glass coverslips for 1 h at room temperature. After polymerization, gels were rehydrated for 45 min and coupled to human plasma fibronectin (FC010, Millipore) for 1 h at room temperature using the photoactivatable cross-linker Sulfo-Sanpah (22589, Pierce

Scientific). Following fibronectin cross-linking, cells were plated on the gels and allowed to spread overnight. The next day, images were taken of both the cells and underlying fluorescent beads. Number of cells imaged per condition: Figure 6B, GFP: 35, CA GFP-RhoA: 27; Figure 6D, 14. Following imaging, cells were removed from the gel using 0.05% SDS and a reference image of the fluorescent beads in the unstrained gel was taken.

Analysis of traction forces was performed using code written in Python according to previously described approaches (Sabass et al., 2008; Hanke et al., 2018). Prior to processing, images were flat-field corrected and the reference bead image was aligned to the bead image with the cell attached. Displacements in the beads were calculated using an optical flow algorithm in OpenCV (Open Source Computer Vision Library, https://github/itseez/opencv) with a window size of 8 pixels. Traction stresses were calculated using the FTTC approach (Butler et al., 2002; Sabass et al., 2008) as previously described, with a regularization parameter of 6.1 \times 10^{-4} . The strain energy was calculated by summing one-half the product of the strain and traction vectors in the region under the cell (Oakes et al., 2014) and normalized by the cell area as measured using the GFP image of the cell.

Quantification of focal adhesion localization

Analysis was performed using custom code written in Python and outlined graphically in Supplemental Figure S5. Briefly, thresholding of the GFP-testin intensity images was performed to create a cell mask. mApple-paxillin intensity images were flat-field corrected and a Laplacian of Gaussian filter was applied for edge detection and creation of a FA mask. FAs were dilated using a 10 × 10 square structuring element and multiplied by the inverted cell mask to create a cytoplasmic doughnut-shaped region surrounding the FAs. The FA mask and surrounding doughnut mask were used to calculate the FA/cytoplasm ratio of the average intensity in the corresponding regions of the testin intensity image. The average FA/cytoplasm ratio was then calculated per cell. Per GFP-testin variant, the total number of cells analyzed was as follows: WT: 49, Y111A: 54, Y111E: 52, Y111F: 52, Y288A: 53, Y288E: 52, Y288F: 44.

Western blotting

Cells were lysed for 20 min on ice in lysis buffer containing 50 mM Tris HCl (pH 7.6), 125 mM NaCl, 5% glycerol, 0.2% NP-40 (ab142227, Abcam), 1.5 mM MgCl₂, and protease and phosphatase inhibitor cocktail (78441, Thermo Scientific). Cell lysates were analyzed using SDS-PAGE and 10% polyacrylamide gels and transferred to a Whatman Protran nitrocellulose membrane (1620115, Biorad). Membranes were blocked for 1 h at room temperature in Odyssey blocking buffer (92740000, LI-COR). After blocking, membranes were incubated at 4°C overnight with primary antibody in Odyssey blocking buffer. Subsequently, membranes were washed three times for 10 min in PBS containing 0.1% Tween 20 (BP337-100, Fisher Scientific) and incubated for 1 h at room temperature with secondary antibody in Odyssey blocking buffer. Finally, membranes were washed three times for 10 min in PBS/Tween 20 and rinsed in Milli-Q-H₂O. The Odyssey Classic infrared imaging device (LI-COR) was used for signal detection. The following primary antibodies were used: mouse anti-GAPDH (MA5-15738, Thermofisher, 1/3000 dilution) and rabbit anti-zyxin (ABD1463, Millipore, 1/1000 dilution), which was a kind gift of Mary Beckerle's laboratory (University of Utah, Salt Lake City, UT). The following LI-COR secondary antibodies were used at a 1/10,000 dilution: goat anti-rabbit IRdye800 (925-32211), goat anti-mouse IRdye680 (925-68070).

Statistical analysis

Statistical analyses were performed in Python using the nonparametric multiple comparison Kruskal–Wallis one-way ANOVA test with Dunn's post hoc method. Details about sample size and *p*-values are included in this section and figure legends.

Software

All images were exported from Slidebook as 16-bit TIFF files and analyzed in Python. All custom code is available at (https://github.com/OakesLab).

ACKNOWLEDGMENTS

We thank the Beach laboratory at the Loyola University Chicago, Maywood, IL for many helpful discussions. We thank the Ampe laboratory at the University of Gent for their critical input and certain testin constructs. We thank Evelyne Friederich and Elisabeth Schaffner-Reckinger from the University of Luxembourg for certain testin constructs. We are also thankful to the Beckerle laboratory at the University of Utah, Salt Lake City, UT for providing us with the zyxin antibody, mcherry-zyxin construct, and both WT and zyxin(-/-) MEFs. This work was supported in part by a National Science Foundation CAREER Award (#2000554) to P.W.O.

REFERENCES

- Blanchoin L, Boujemaa-Paterski R, Sykes C, Plastino J (2014). Actin dynamics, architecture, and mechanics in cell motility. Physiol Rev 94, 235–263.
- Boëda B, Briggs DC, Higgins T, Garvalov BK, Fadden AJ, McDonald NQ, Way M (2007). Tes, a specific mena interacting partner, breaks the rules for EVH1 binding. Mol Cell 28, 1071–1082.
- Boëda B, Knowles PP, Briggs DC, Murray-Rust J, Soriano E, Garvalov BK, McDonald NQ, Way M (2011). Molecular recognition of the Tes LIM2-3 domains by the actin-related protein Arp7A. J Biol Chem 286, 11543–11554.
- Brown AEX, Discher DE (2009). Conformational changes and signaling in cell and matrix physics. Curr Biol 19, R781–R789.
- Butler JP, Toli-Nørrelykke IM, Fabry B, Fredberg JJ (2002). Traction fields, moments, and strain energy that cells exert on their surroundings. Am J Physiol - Cell Physiol 282, 595–605.
- Cai Y, Sheetz MP (2009). Force propagation across cells: mechanical coherence of dynamic cytoskeletons. Curr Opin Cell Biol 21, 47–50.
- Chartier L, Rankin LL, Allen RE, Kato Y, Fusetani N, Karaki H, Watabe S, Hartshorne DJ (1991). Calyculin-A increases the level of protein phosphorylation and changes the shape of 3T3 fibroblasts. Cell Motil Cytoskeleton 18, 26–40.
- Das T, Safferling K, Rausch S, Grabe N, Boehm H, Spatz JP (2015). A molecular mechanotransduction pathway regulates collective migration of epithelial cells. Nat Cell Biol 17, 276–287.
- Drusco A, Zanesi N, Roldo C, Trapasso F, Farber JL, Fong LY, Croce CM (2005). Knockout mice reveal a tumor suppressor function for testin. Proc Natl Acad Sci USA 102, 10947–10951.
- Engler AJ, Sen S, Sweeney HL, Discher DE (2006). Matrix elasticity directs stem cell lineage specification. Cell 126, 677–689.
- Fabry B, Fredberg JJ (2007). Mechanotransduction, asthma and airway smooth muscle. Drug Discov Today Dis Model 4, 131–137.
- Feng J, Lucchinetti E, Enkavi G, Wang Y, Gehrig P, Roschitzki B, Schaub MC, Tajkhorshid E, Zaugg K, Zaugg M (2010). Tyrosine phosphorylation by Src within the cavity of the adenine nucleotide translocase 1 regulates ADP/ATP exchange in mitochondria. Am J Physiol - Cell Physiol 298, 740–748.
- Garvalov BK, Higgins TE, Sutherland JD, Zettl M, Scaplehorn N, Köcher T, Piddini E, Griffiths G, Way M (2003). The conformational state of Tes regulates its zyxin-dependent recruitment to focal adhesions. J Cell Biol 161, 33–39.
- Gill GN (1995). The enigma of LIM domains. Structure 3, 1285–1289. Goldmann WH (2016). Role of vinculin in cellular mechanotransduction. Cell Biol Int 40, 241–256.
- Griffith E, Coutts AS, Black DM (2004). Characterisation of chicken TES and its role in cell spreading and motility. Cell Motil Cytoskeleton 57, 133–142.

- Gu Z, Ding G, Liang K, Zhang H, Guo G, Zhang L, Cui J (2014). TESTIN suppresses tumor growth and invasion via manipulating cell cycle progression in endometrial carcinoma. Med Sci Monit 20, 980–987.
- Guizar-sicairos M, Thurman ST, Fienup JR (2008). Efficient subpixel image registration algorithms. Opt Lett 33, 156–158.
- Haining AWM, Lieberthal TJ, Del Río Hernández A (2016). Talin: a mechanosensitive molecule in health and disease. FASEB J 30, 2073–2085.
- Hanke J, Probst D, Zemel A, Schwarz US, Köster S (2018). Dynamics of force generation by spreading platelets. Soft Matter 14, 6571–6581.
- Hemmatian H, Bakker AD, Klein-Nulend J, van Lenthe GH (2017). Aging, osteocytes, and mechanotransduction. Curr Osteoporos Rep 15, 401–411.
- Heydemann A, McNally EM (2007). Consequences of disrupting the dystrophin-sarcoglycan complex in cardiac and skeletal myopathy. Trends Cardiovasc Med 17, 55–59.
- Hoffman LM, Jensen CC, Chaturvedi A, Yoshigi M, Beckerle MC (2012). Stretch-induced actin remodeling requires targeting of zyxin to stress fibers and recruitment of actin regulators. Mol Biol Cell 23, 1846–1859.
- Iskratsch T, Wolfenson H, Sheetz MP (2014). Appreciating force and shape the rise of mechanotransduction in cell biology. Nat Rev Mol Cell Biol 15, 825–833.
- Jégou A, Romet-Lemonne G (2021). Mechanically tuning actin filaments to modulate the action of actin-binding proteins. Curr Opin Cell Biol 68, 72–80.
- Kanchanawong P, Shtengel G, Pasapera AM, Ramko EB, Davidson MW, Hess HF, Waterman CM (2010). Nanoscale architecture of integrin-based cell adhesions. Nature 468, 580–584.
- Koch BJ, Ryan JF, Baxevanis AD (2012). The diversification of the lim superclass at the base of the metazoa increased subcellular complexity and promoted multicellular specialization. PLoS One 7. doi:10.1371/journal. pone.0033261.
- Kong F, García AJ, Mould AP, Humphries MJ, Zhu C (2009). Demonstration of catch bonds between an integrin and its ligand. J Cell Biol 185, 1275–1284
- Le S, Hu X, Yao M, Chen H, Yu M, Xu X, Nakazawa N, Margadant FM, Sheetz MP, Yan J (2017). Mechanotransmission and mechanosensing of human alpha-actinin 1. Cell Rep 21, 2714–2723.
- Lecuit T, Lenne PF, Munro E (2011). Force generation, transmission, and integration during cell and tissue morphogenesis. Annu Rev Cell Dev Biol 27, 157–184.
- Lemmon CA, Chen CS, Romer LH (2009). Cell traction forces direct fibronectin matrix assembly. Biophys J 96, 729–738.
- Lessey EC, Guilluy C, Burridge K (2012). From mechanical force to RhoA activation. Biochemistry 51, 7420–7432.
- Li H, Huang K, Gao L, Wang L, Niu Y, Liu H, Wang Z, Wang L, Wang G, Wang J (2016). TES inhibits colorectal cancer progression through activation of p38. Oncotarget 7, 45819–45836.
- Nishi H, Hashimoto K, Panchenko AR (2011). Phosphorylation in protein–protein binding: effect on stability and function. Structure 19, 1807–1815.
- Oakes PW, Banerjee S, Marchetti MC, Gardel ML (2014). Geometry regulates traction stresses in adherent cells. Biophys J 107, 825–833.
- Oakes PW, Bidone TC, Beckham Y, Skeeters AV, Ramirez-San Juan GR, Winter SP, Voth GA, Gardel ML (2018). Lamellipodium is a myosin-independent mechanosensor. Proc Natl Acad Sci USA 115, 2646–2651.
- Oakes PW, Gardel ML (2014). Stressing the limits of focal adhesion mechanosensitivity. Curr Opin Cell Biol 30, 68–73.
- Oakes PW, Wagner E, Brand CA, Probst D, Linke M, Schwarz US, Glotzer M, Gardel ML (2017). Optogenetic control of RhoA reveals zyxin-mediated elasticity of stress fibres. Nat Commun 8. doi:10.1038/ncomms15817.
- Ohashi K, Fujiwara S, Mizuno K (2017). Roles of the cytoskeleton, cell adhesion and rho signalling in mechanosensing and mechanotransduction. J Biochem 161, 245–254.
- Oldenburg J, Van Der Krogt G, Twiss F, Bongaarts A, Habani Y, Slotman JA, Houtsmuller A, Huveneers S, De Rooij J (2015). VASP, zyxin and TES are tension-dependent members of focal adherens junctions independent of the α -catenin-vinculin module. Sci Rep 5, 1–14.
- Paluch EK, Nelson CM, Biais N, Fabry B, Moeller J, Pruitt BL, Wollnik C, Kudryasheva G, Rehfeldt F, Federle W (2015). Mechanotransduction: use the force(s). BMC Biol 13, 1–14.
- Paszek MJ, Zahir N, Johnson KR, Lakins JN, Rozenberg GI, Gefen A, Reinhart-King CA, Margulies SS, Dembo M, Boettiger D, et al. (2005). Tensional homeostasis and the malignant phenotype. Cancer Cell 8, 241–254.
- Payne-Tobin Jost A, Waters JC (2019). Designing a rigorous microscopy experiment: validating methods and avoiding bias. J Cell Biol 218, 1452–1466.

- Prager-Khoutorsky M, Lichtenstein A, Krishnan R, Rajendran K, Mayo A, Kam Z, Geiger B, Bershadsky AD (2011). Fibroblast polarization is a matrix-rigidity-dependent process controlled by focal adhesion mechanosensing. Nat Cell Biol 13, 1457–1465.
- Rauskolb C, Sun S, Sun G, Pan Y, Irvine KD (2014). Cytoskeletal tension inhibits Hippo signaling through an Ajuba–Warts complex. Cell 158, 143–156.
- Ridley AJ, Hall A (1992). The small GTP-binding protein rho regulates the assembly of focal adhesions and actin stress fibers in response to growth factors. Cell 70, 389–399.
- Sabass B, Gardel ML, Waterman CM, Schwarz US (2008). High resolution traction force microscopy based on experimental and computational advances. Biophys. J 94, 207–220.
- Sala S, Ampe C (2018). An emerging link between LIM domain proteins and nuclear receptors. Cell Mol Life Sci 75, 1959–1971.
- Sala S, Catillon M, Hadzic E, Schaffner-Reckinger E, Van Troys M, Ampe C (2017a). The PET and LIM1-2 domains of testin contribute to intramolecular and homodimeric interactions. PLoS One 12, 1–21.
- Sala S, Van Troys M, Medves S, Catillon M, Timmerman E, Staes A, Schaffner-Reckinger E, Gevaert K, Ampe C (2017b). Expanding the interactome of TES by exploiting TES modules with different subcellular localizations. J Proteome Res 16, 2054–2071.
- Sarti M, Sevignani C, Calin GA, Aqeilan R, Shimizu M, Pentimalli F, Picchio MC, Godwin A, Rosenberg A, Drusco A, et al. (2005). Adenoviral transduction of TESTIN gene into breast and uterine cancer cell lines promotes apoptosis and tumor reduction in vivo. Clin Cancer Res 11, 806–813.
- Schwarz US, Gardel ML (2012). United we stand—integrating the actin cytoskeleton and cell-matrix adhesions in cellular mechanotransduction. J Cell Sci 125, 3051–3060.
- Smith M, Hoffman L, Beckerle M (2014). LIM proteins in actin cytoskeleton mechanoresponse. Trends Cell Biol 24, 575–583.
- Smith MA, Blankman E, Deakin NO, Hoffman LM, Jensen CC, Turner CE, Beckerle MC (2013). LIM domains target actin regulators paxillin and zyxin to sites of stress fiber strain. PLoS One 8, e69378.
- Smith MA, Blankman E, Gardel ML, Luettjohann L, Clare M, Beckerle MC (2011). A zyxin-mediated mechanism for actin stress fiber maintenance and repair. Dev Cell 19, 365–376.
- Stricker J, Aratyn-schaus Y, Oakes PW, Gardel ML (2011). Spatiotemporal constraints on the force-dependent growth of focal adhesions. Biophysj 100, 2883–2893.
- Sun X, Phua DYZ, Axiotakis L, Smith MA, Blankman E, Gong R, Cail RC, Espinosa de los Reyes S, Beckerle MC, Waterman CM, Alushin GM (2020). Mechanosensing through direct binding of tensed F-actin by LIM domains. Dev Cell 55, 468–482.e7.
- Sun Z, Guo SS, Fässler R (2016). Integrin-mediated mechanotransduction. J Cell Biolournal Cell Biol 215, 445–456.
- Suzuki W, Ichikawa K, Ohki T, Kohno Y, Sata M, Nose K, Shibanuma M (2005). Uni-axial stretching regulates intracellular localization of Hic-5 expressed in smooth-muscle cells in vivo. J Cell Sci 118, 937–949.
- Svitkina T (2018). The actin cytoskeleton and actin-based motility. Cold Spring Harb Perspect Biol 10, 1–22.
- Tobias ES, Hurlstone AFL, MacKenzie E, Mcfarlane R, Black DM (2001). The TES gene at 7q31.1 is methylated in tumours and encodes a novel growth-suppressing LIM domain protein. Oncogene 20, 2844–2853.
- Tojkander S, Gateva G, Lappalainen P (2012). Actin stress fibers—assembly, dynamics and biological roles. J Cell Sci 125, 1855–1864.
- Torsoni AS, Marin TM, Velloso LA, Franchini KG (2005). RhoA/ROCK signaling is critical to FAK activation by cyclic stretch in cardiac myocytes. Am J Physiol Hear Circ Physiol 289, 1488–1496.
- Winkelman JD, Anderson ĆA, Suarez C, Kovar DR, Gardel ML (2020). Evolutionarily diverse LIM domain-containing proteins bind stressed actin filaments through a conserved mechanism. Proc Natl Acad Sci USA 117, 25532–25542
- Yoshigi M, Hoffman LM, Jensen CC, Yost HJ, Beckerle MC (2005). Mechanical force mobilizes zyxin from focal adhesions to actin filaments and regulates cytoskeletal reinforcement. J Cell Biol 171, 209–215.
- Zaidel-Bar R, Itzkovitz S, Ma'ayan A, Iyengar R, Geiger B (2007). Functional atlas of the integrin adhesome Ronen. Nat Cell Biol 9, 858–867.
- Zhu J, Li X, Kong X, Moran MS, Su P, Haffty BG, Yang Q (2012). Testin is a tumor suppressor and prognostic marker in breast cancer. Cancer Sci 103, 2092–2101.
- Zimmermann D, Homa KE, Hocky GM, Pollard LW, De La Cruz EM, Voth GA, Trybus KM, Kovar DR (2017). Mechanoregulated inhibition of formin facilitates contractile actomyosin ring assembly. Nat Commun 8, 1–12.